Electron trapping/detrapping at oxygen vacancies and imprint evolution in La-doped $Hf_{0.5}Zr_{0.5}O_2$ ferroelectric capacitors probed by hard X-ray photoelectron spectroscopy

W. Hamouda,[1, a)] Y. Yamashita,[2] S. Ueda,[2, 3] S. Matzen,[4] O. Renault,[5] F. Mehmood,[6, b)] T. Mikolajick,[6] U. Schroeder,[6] and N. Barrett[1]

[1)] *SPEC, CEA, CNRS, Université Paris-Saclay, CEA Saclay, 91191 Gif-sur-Yvette, France*
[2)] *Research Center for Electronic and Optical Materials, National Institute for Materials Science (NIMS), Namiki, Tsukuba 305-0044, Japan*
[3)] *Synchrotron X-ray Station at SPring-8, National Institute for Materials Science, Sayo, Hyogo 679-5148, Japan*
[4)] *C2N, CNRS, Paris-Saclay University, 91120 Palaiseau, France*
[5)] *Univ. Grenoble Alpes, CEA, Leti, F-38000 Grenoble, France*
[6)] *NaMLab gGmbH/TU Dresden, Nöthnitzer Str. 64a, 01187 Dresden, Germany*

(*Correspondence should be addressed to nick.barrett@cea.fr)

(Dated: 13 October 2025)

We evaluate the correlation between polarization-dependent oxygen vacancy profile and imprint in technologically relevant TiN/La doped $Hf_{0.5}Zr_{0.5}O_2$/TiN ferroelectric capacitors using hard X-ray photoelectron spectroscopy (HAXPES) with *in-situ* biasing. The concentration of double positively charged oxygen vacancies ($V_{\ddot{O}}$) was inferred from the intensity of reduced hafnium (Hf^{3+}, ($5d^1$)) in the Hf $3d_{5/2}$ spectra, relative to fully oxidized (Hf^{4+}, ($5d^0$)). HAXPES was performed using two photon energies to discriminate $V_{\ddot{O}}$ near the top interface from those averaged over the whole film. The evolution of imprint with time and the extracted activation energy of ∼0.1 eV strongly support a fast, low-barrier electronic process such as shallow charge trapping/detrapping, rather than field induced vacancy drift. On the ∼30 min timescale after polarization reversal, we propose that the $V_{\ddot{O}}$ deduced from HAXPES reflects a polarization-driven snapshot of the defect charge state ($V_O^x \leftrightarrow V_{\ddot{O}}$), rather than a change in the physical vacancy density previously reported. Following polarization reversal, electrons redistribute between vacancy levels and Hf $5d$ orbitals. This is correlated with $Hf^{4+} \leftrightarrow Hf^{3+}$ transitions, leading to $0 \leftrightarrow 2+$ vacancy charge state modifying the local electronic environment and screening behavior, particularly near interfaces. From the Schottky barrier height change due to polarization reversal, an effective screening length of 0.04 Å was estimated for the top interface. The results reveal a dominant role of polarization-dependent electron trapping/detrapping, partially screening ferroelectric polarization charges, thereby stabilizing one remanent state over the other.

Keywords: ferroelectric $Hf_{0.5}Zr_{0.5}O_2$, HAXPES, imperfect screening, depolarizing field, polarization imprint, oxygen vacancy (V_O), charge trapping/detrapping

Research on hafnia-based ferroelectric capacitors (FeCAPs) has been intensified since the discovery of ferroelectricity in HfO_2-based materials due to their potential applications for low-power non-volatile memories and memristive devices[1–5]. In this context, the main reliability parameters are endurance, retention, and imprint[6].

Field cycling is usually necessary to fully unpin the ferroelectric domains and reach optimal polarization. Endurance is the number of cycles before fatigue sets in with closure of the memory window, increase in leakage current and finally hard breakdown. Retention measures the ferroelectric state stability over time, typically at 85°C for consumer electronics. Reported time-scales of $\sim 10^5$s must be extrapolated to 10 years for commercial applications[7–9].

Oxygen vacancies (V_O) are known to impact endurance and retention[9–12]. In addition to stabilizing the polar orthorhombic structure at modest concentrations and providing conductivity paths at higher concentrations, they act as electron traps with shallow charged levels ($V_{\ddot{O}}$) located typically 0.3–0.5 eV below the conduction band minimum (CBM), and deep neutral levels (V_O^x) positioned 2-3 eV below the CBM[9,12,13]. Retention is also closely connected to imprint which manifests itself as a time and temperature dependent shift of the polarization-voltage hysteresis loop along the voltage axis, destabilizing one state with respect to the other. The incomplete screening of the polarization bound charges results in a depolarizing field (E_{dep}) in the ferroelectric layer and a field at the ferroelectric/electrode interface. These fields result in a time-dependent redistribution of charge via a variety of mechanisms, including bulk charge transport, charge injection at the interfaces, trapping/detrapping at defect sites, giving rise to the imprint field, E_{imp}. In addition, asymmetric electrodes or interface chemistry will result in asymmetric polarization screening further modulating E_{imp}[14].

To describe the polarization screening at the metal interface, an effective screening length, λ_{eff}, is used[15,16]. λ_{eff} is generally regarded as the width of the screening charge distribution in the metal electrode and therefore depends on the elec-

[a)] Present address: Helmholtz-Zentrum Berlin für Materialien und Energie, Hahn-Meitner-Platz 1, 14109 Berlin, Germany
[b)] Present address: GlobalFoundries Dresden, Wilschdorfer Landstr. 101, 01109 Dresden, Germany

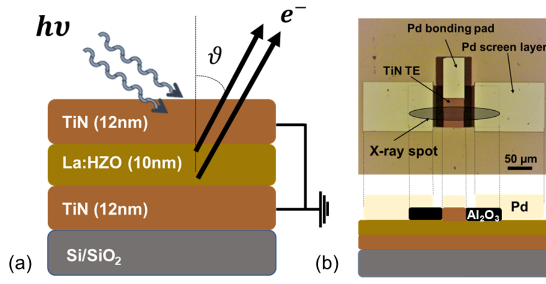

FIG. 1. (a) Schematic of the analyzed stack highlighting the probing depth using two distinct photon energies (b) Optical image (top) and cross section (bottom) of a single device dedicated for HAXPES with *in-situ* biasing.

trode material, the defect state of the interfacial region i.e. the specific interface chemistry and the polarization magnitude. It can be deduced from the Schottky barrier height (SBH) change ($\Delta\varphi_{(\mathrm{B,n})}$) (in eV) due to polarization reversal[15,17]:

$$\Delta\varphi_{(\mathrm{B,n})} = 2\lambda_{\mathrm{eff}} P_{\mathrm{r}}/\varepsilon_0 \quad (1)$$

where P_{r} stands for the remanent polarization value and ε_0 for the vacuum permittivity.

Laboratory X-ray photoelectron spectroscopy (XPS) can provide direct quantitative information on defects and band alignment. By assuming that each V_O^x releases two electrons reducing two Hf ions from 4+ to 3+ state, the double positively charged $V_{\ddot{O}}$ concentration can be estimated from the $I(Hf^{3+})/ [(I(Hf^{3+}) + I(Hf^{4+})]$ intensity ratio. The shift in the core level binding energy can be used to estimate $\Delta\varphi_{(B,n)}$ and thus λ_{eff}[18,19]. X-rays produced by synchrotron radiation in a hard X-ray photoelectron spectroscopy (HAXPES) experiment probing the same core levels increase significantly the photoelectron inelastic mean free path and thus the probing depth with respect to laboratory based XPS[20]. This allows studying the ferroelectric layer in realistic device structures in a non-invasive manner[17,18,21,22].

Recent studies have highlighted the role of electronic charge injection and/or trapping/detrapping at the metal/ferroelectric interface as a key contributor to imprint formation at room temperature[14]. This charge movement is driven by the built-in fields E_{dep} and the interfacial electric field, however, the kinetics depend on the activation energy, i.e. the potential barrier to each mechanism. In the case of charge trapping/detrapping at point defects such as V_O, the equilibrium concentration of the latter is determined by the total energy of the system in a given polarization state. In the vicinity of electrodes, low-permittivity interfacial layers (IL) generate increased electric fields, further modulating charge redistribution and resulting in time-dependent imprint fields, as discussed in the "fluid imprint" model[23–26].

In this work, we investigate the imprint and its underlying mechanisms in fully woken-up TiN/La:$Hf_{0.5}Zr_{0.5}O_2$/TiN ferroelectric capacitors using HAXPES combined with electrical measurements. While the $V_{\ddot{O}}$ signature in HAXPES has previously been used to assess static oxygen vacancy concentra-

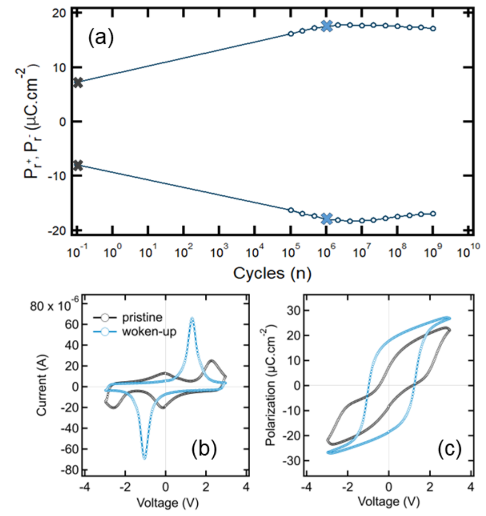

FIG. 2. (a) Endurance plot and (b) I - V, (c) P - V responses of pristine (black) and woken-up, after 10^6 cycles (blue) TiN/HZLO/TiN capacitors.

tion, our results reveal that on short time scale after polarization reversal (30 minutes at room temperature), polarization-dependent variations in the $V_{\ddot{O}}$ (Hf^{3+}) signal can also reflect the number of electrons trapped at V_O sites. The extracted activation energy of ∼0.1 eV for the polarization imprint and the polarization-dependent variation in Hf^{3+}/Hf_{tot} photoemission signal indicate a fast, low-barrier electronic process rather than slower V_O migration.

TiN/La:$Hf_{0.5}Zr_{0.5}O_2$(HZLO)/TiN ferroelectric capacitors were fabricated on p-doped Si(100) substrates. The La concentration is 2.3 mol%, achieved by modulating the La/(Hf + Zr) atomic layer deposition cycle ratios and growth rates accordingly. Crystallization of the 10 nm HZLO film in the desired polar orthorhombic phase was achieved by rapid thermal annealing at 500°C for 20 s in a N_2 atmosphere after the deposition of the 12 nm TiN top electrode and verified by grazing incidence X-ray diffraction%[8]. 100×100 μm^2 devices were then patterned for HAXPES analysis with *in-situ* applied bias. Figure. 1 shows a schematic cross-section of the capacitor stack and an optical image of the device. For biasing, capacitors are connected via bonding pads to gold contacts on the sample holder. Capacitors were cycled *ex-situ* to woken-up states using an aixACCT TF 1000 ferrotester using 100 kHz square pulses with ±3 V amplitude. Hysteresis loops were measured at various cycling stages using ±3 V triangular pulses at 1 kHz (Fig. 2). In the pristine state, a typical pinched, antiferroelectric-like hysteresis curve is observed. Cycling to 10^6 cycles results in the unpinching of the hysteresis, an increase of the $2P_r$ value from 16 to 35 $\mu C.cm^{-2}$ and a 1.1 - 1.3 V coercive voltage (V_C).

For the imprint experiment, woken-up capacitors were polarized in $P^{\uparrow}$ (pointing toward the top electrode) and $P^{\downarrow}$ (toward the bottom electrode) states. The capacitors were then held for different durations at room temperature. The current-voltage (I-V) and the resulting polarization-voltage (P-V)

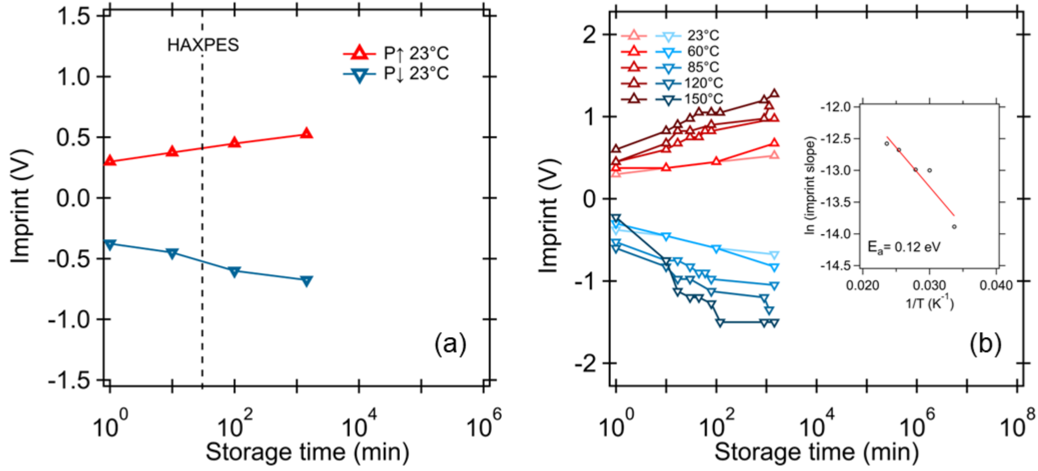

FIG. 3. Positive (red) and negative (blue) time-dependent imprint corresponding to $P^{\uparrow}$ and $P^{\downarrow}$ stored states from 1min to 3hrs at (a) room temperature and (b) at different temperatures allowing the extraction of the activation energy. The dotted line in (a) indicates the time of the HAXPES analysis. The Arrhenius plot is shown in the inset of (b).

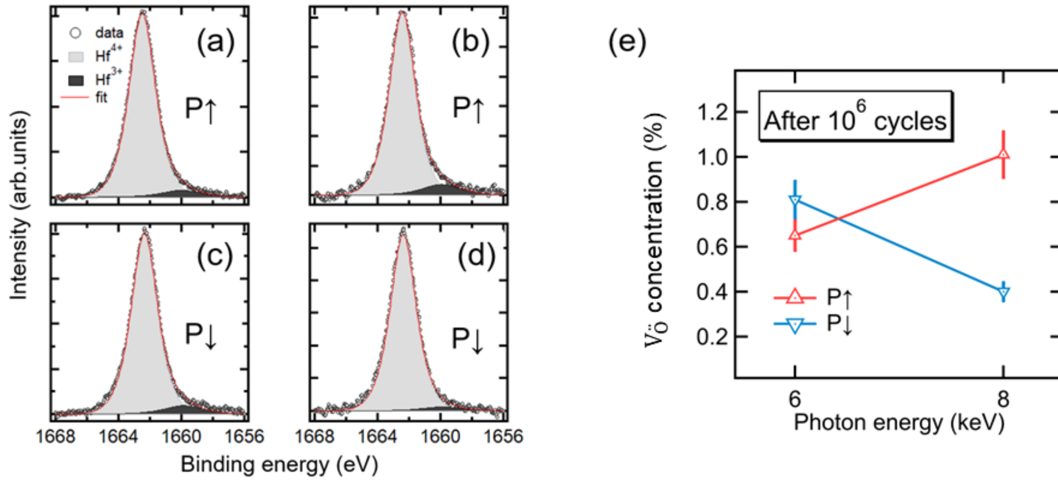

FIG. 4. Polarization dependent Hf $3d_{5/2}$ spectra at 6 keV (a,c) and 8 keV (b,d) photon energy in woken up capacitors (e) Estimated oxygen vacancy concentration ($V_{\ddot{O}}$) as a function of probing depth for $P^{\uparrow}$ and $P^{\downarrow}$ remanent states.

curves were measured with a triangular pulse train (±3 V/10 μs) so that the initial stored state is always maintained after the measurement.

HAXPES measurements were conducted on the BL15XU beamline of SPring-8[27]. Photon energies of 6 and 8 keV were selected using a double-crystal Si (111) monochromator (DCM) and a post-monochromator channel-cut Si (333) crystal. This gives a total energy resolution at room temperature of 250 and 280 meV, respectively, determined by extracting the 16/84% width of the Fermi edge of a grounded gold reference sample, also used for binding energy calibration. Photoelectrons were detected using an hemispherical analyzer (VG Scienta, R4000) with an emission angle (θ) of 35° with respect to the sample surface normal. The sampling depth using Hf $3d_{5/2}$ photoelectrons is defined as $3\lambda\cos\theta$ (corresponding to 95% of total intensity), with λ representing the kinetic energy-dependent inelastic mean free path (IMFP) of the selected photoelectrons through the top TiN electrode. The IMFP were calculated using the Tanuma, Powell, and Penn (TPP-2M) algorithm implemented in the QUASES software[28] to be ~6 and 8.5 nm using 6 and 8 keV excitation energies, yielding sampling depths of 15±0.8 (6 keV) and 21±1.1 nm (8 keV). Analysis of the spectra was performed using CasaXPS software[29]. A Shirley background was used to simulate the secondary electron background and pseudo-Voigt (Gaussian/Lorentzian with 70% Lorentzian character) function was used to fit the spectra. *In-situ* polarization switching was performed using a triangular pulse (±3 V/10 μs) with a KEYSIGHT 33512B waveform generator. HAXPES measurements were recorded ~30 min after the pulse application in short-circuit conditions.

Figure 3(a) shows the evolution of imprint voltage ((V_C^+

- V_C^-)/2, where V_C^+ and V_C^- are the coercive voltages) with time for the $P^{\uparrow}$ and $P^{\downarrow}$ states at room temperature, measured over a 3 hour period. The imprint field evolves toward +0.4 $MV.cm^{-1}$ for $P^{\uparrow}$ and -0.5 $MV.cm^{-1}$ for $P^{\downarrow}$ within the first 30 min, coinciding with the timing of the HAXPES measurements. The imprint increases over time, reflects the time-dependent built-in internal field (E_{imp}) that differentiates the two remanent states and stabilizes the previously programmed state. Figure 3(b) presents the temperature dependence of the imprint evolution for five different temperatures from room temperature to 150°C . The extracted activation energy from the Arrhenius plot of ln(imprint slope) versus 1/T is 0.12 eV (inset) is significantly lower than typical migration barrier for oxygen vacancies ($\sim$1 eV)[30]. This strongly indicates that the dominant mechanism behind the initial imprint formation is not bulk $V_{\ddot{O}}$ migration but a much faster process. Specifically, we suggest that the initial imprint evolution is due to charge trapping and detrapping of electrons at V_O sites.

HAXPES was used to evaluate the Hf^{3+} distribution as a function of polarization state in the woken up state in order to evaluate the $V_{\ddot{O}}$ concentration at a characteristic time (30 minutes) during the imprint evolution shown in Fig. 3(a). Figure 4 shows the polarization dependent Hf $3d_{5/2}$ spectra at (a,c) 6 and (b,d) 8 keV photon energies. Spectra are fitted by two peaks: Hf^{4+} (gray) and Hf^{3+} (black)[24,31]. The two peak fit is detailed in Supplemental Material. We estimate the $V_{\ddot{O}}$ concentration from the intensity ratio using $1/8\times I(Hf^{3+})/I(Hf_{tot})$[32]. The results are plotted as a function of the photon energy in Fig. 4(e) for $P^{\uparrow}$ and $P^{\downarrow}$ states. At the top interface the $V_{\ddot{O}}$ concentration is higher in the $P^{\downarrow}$ state (0.81%) than in the $P^{\uparrow}$ state (0.65%) whereas deeper into the film the situation is reversed, 1.01% and 0.40% for $P^{\uparrow}$ and $P^{\downarrow}$ states, respectively. The $\sim$0.4% $V_{\ddot{O}}$ difference between the top interface and the bulk (6 vs. 8 keV) indicates a significant profile of $V_{\ddot{O}}$ across the stack, not necessarily expected in woken-up devices[33–35].

The $V_{\ddot{O}}$ gradient for $P^{\uparrow}$ and $P^{\downarrow}$ derived from HAXPES (Fig. 4(e)) is qualitatively consistent with the direction of E_{dep} and the measured E_{imp} (imprint) set by the remanent polarization ($E(z) = -\frac{d\phi}{dz}$), but not necessarily indicative of large-scale vacancy drift over the 30 min timescale, suggesting that the observed $V_{\ddot{O}}$-related signal modulation may originate primarily from a modulation of their charge state rather than physical migration.

At 6 keV, when polarization points downward, resulting in negative bound charge at the top interface, electrostatic considerations would normally favor more positively charged oxygen vacancies[36]. However, the higher $V_{\ddot{O}}$ content at the top interface in $P^{\downarrow}$ (compared to $P^{\uparrow}$) cannot simply be explained on such a short timescale by $V_{\ddot{O}}$ migration, since the latter has an activation energy about one order of magnitude higher than the measured value ($\sim$0.1 eV). The combined HAXPES and electrical measurements indicate that the $V_{\ddot{O}}$ signal reflects polarization-dependent modulation of the vacancy charge state and the associated valency of neighboring Hf ions. For $P^{\downarrow}$, electron detrapping from pre-existing neutral vacancies (V_O^x) converts them into doubly ionized ($V_{\ddot{O}}$), forming $V_{\ddot{O}}$-Hf^{3+} complexes via transfer of the released electrons onto neighboring Hf 5*d* orbitals ($5d^1$). This increases the measured Hf^{3+} fraction. For $P^{\uparrow}$, on the contrary, electron trapping at $V_{\ddot{O}}$ results in the formation of V_O^x-Hf^{4+} complexes by depopulating the Hf 5*d* orbitals (Hf^{3+} ($5d^1$) $\rightarrow$ Hf^{4+} ($5d^0$)), i.e. electron transfer from Hf^{3+} to $V_{\ddot{O}}$ to form an Hf^{4+}-V_O^X complex. This reduces the Hf^{3+} signal and weakens the contribution from vacancy-related electronic screening. In both polarization states, the balance between $V_{\ddot{O}}$-Hf^{3+} and V_O^x-Hf^{4+} complexes near the top electrode is determined by the total energy of the system, $V_{\ddot{O}}$ having a lower energy near to negative bound polarization charge. E_{dep} contributes to providing a driving force for redistribution of charge, but the $V_{\ddot{O}}$ kinetics are limited by the high activation energy. In this picture, electron trapping/detrapping processes are essentially local, and do not imply long-range "conduction-like" electron transport across the ferroelectric film.

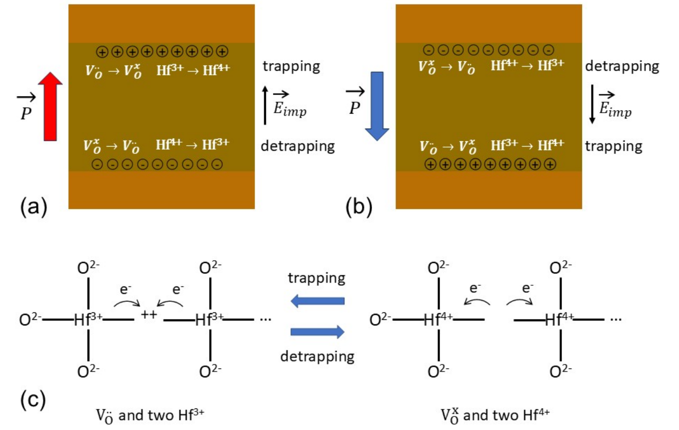

FIG. 5. Schematic illustration of the polarization-dependent redistribution of trapped electrons and the resulting depth-dependent oxygen vacancy charge state in La-doped $Hf_{0.5}Zr_{0.5}O_2$ capacitors under (a) $P^{\uparrow}$ and (b) $P^{\downarrow}$ remanent polarization. Over the 30-minute timescale of this study, the ionic drift response is expected to be limited. Instead, the polarization discontinuity at the interfaces enhances charge redistribution. In $P^{\uparrow}$ state electrons are trapped at $V_{\ddot{O}}$ near the top interface and detrapped from neutral V_O^X at the bottom interface. The opposite process occurs in the $P^{\downarrow}$ state. (c) Suggested exchange between $V_{\ddot{O}}$-Hf^{3+} and V_O^x-Hf^{4+} defects by trapping/detrapping.

The 8 keV spectra, which probe the entire ferroelectric thickness, show a markedly higher $V_{\ddot{O}}$ fraction for P↑ than P↓ (Fig. 4e). If the total vacancy population remains constant on the $\sim$30 min timescale, these changes are attributed to negative bound polarization charge at the top interface (P↓) promoting detrapping and vacancy ionization, while positive bound charge at the bottom interface (P↓) favor vacancy neutralization. The opposite applies for P↑ at both interfaces and the scenario is consistent with the low activation energy extracted from imprint kinetics, pointing to a fast, low-barrier electronic mechanism rather than slow ionic drift.

The Supplemental Material includes a quantitative depth-profile simulation of $V_{\ddot{O}}$ based on Hf^{3+} fractions from the experimental 6 and 8 keV measurements. Modeling the 10

nm film as five, 2 nm sublayers, and assuming a linear electrostatic potential profile within the HZLO film with magnitudes and sign derived from the experimental imprint results presented in Fig. 3(a), shows that the 0.6% difference in the averaged 8 keV measurement between P↑ and P↓ translates into a much larger contrast in the vicinity of the bottom interface: ∼1.2% difference (∼1.20% for P↑ and ∼0.01% for P↓). The predicted depth concentration profile reinforces the proposed mechanism: electron detrapping from V_O^X near negative polarization charges boosts $V_{\ddot{O}}$-Hf^{3+} fraction, while electron trapping at $V_{\ddot{O}}$ near positive polarization charges favors V_O^x-Hf^{4+}, reducing $V_{\ddot{O}}$ for better screening efficiency. Indeed, $V_{\ddot{O}}$ prefer energetically being in proximity to negative polarization charge[36].

Previous studies under more static conditions (typically several days to weeks after poling) have demonstrated that the Hf^{3+}/Hf_{tot} ratio can be used to accurately quantify the fixed $V_{\ddot{O}}$ concentration changes induced by electrode material, doping, or annealing conditions[24,37,38], and to evaluate $V_{\ddot{O}}$ drift over longer timescales[39,40]. Our findings indicate that this spectroscopic signature, on shorter timescales (here 30 min after poling), also reflects a snapshot of charge occupancy variation, under E_{dep}. The ∼0.1 eV activation energy strongly suggests that shallow electron trapping/detrapping dominates the early imprint evolution, consistent with prior findings[7,9]. Shvilberg *et al*[30] reported a diffusion coefficient of 10^{-18} $cm^2.s^{-1}$ for oxygen vacancies with an activation energy of 1 eV, corresponding to an average migration distance of only 1 nm over 3 hrs. One must also consider the possibility of electron injection from the electrode under negative bias. In order to assess the possibility of charge injection, we have calculated the SBH from the core level spectra.

The SBH is the offset between the conduction band edge of HZLO and the Fermi level of the metal electrode. Figure 6 shows the bias induced displacements of the Hf $3d_{5/2}$. The spectra shift towards E_F by 300 meV when switching from $P^{\uparrow}$ to $P^{\downarrow}$. The grounded Ti 1*s* spectra from the top electrode are also included providing the binding energy reference and, as expected, shows no shift, confirming the metallic nature.

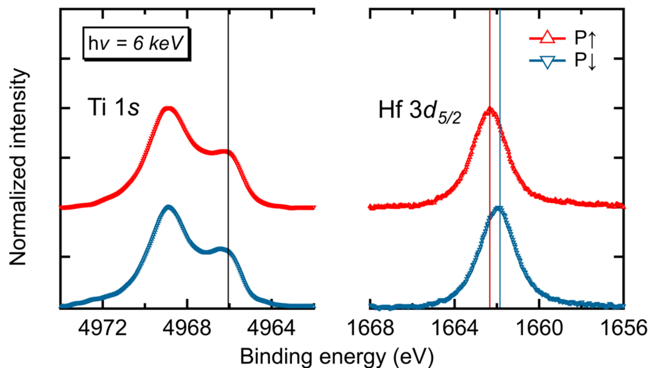

FIG. 6. Polarization-induced band shifts near top interface as detected on the Ti 1*s* and Hf $3d_{5/2}$ emission lines at 6 keV.

The SBH deduced from Fig. 6 are 2.55 eV for $P^{\uparrow}$ and 2.85 eV for $P^{\downarrow}$, respectively (see Supplemental Material). The measured top SBH and the imprint-derived internal field after 30 min (∼0.4-0.5 $MV.cm^{-1}$) imply that, at 0 V, the interfacial layer field is ∼2.0–2.5 $MV.cm^{-1}$ ($\varepsilon_{HZLO}/\varepsilon_{IL}$∼5), insufficient for significant thermionic or Fowler–Nordheim injection. We can therefore exclude charge injection as the principal origin of the imprint change on the experimental timescale. As shown in Fig. 2, the measured current around 1.5 V is dominated by switching and dielectric contributions, while the leakage remains very low and does not increase significantly even up to 3 V. This suggests that any fresh charge injection or field-assisted transient tunneling is restricted to the ms time window of the polarization pulse and likely sets the initial trap occupancy, but cannot explain the imprint evolution with time[7]. At longer timescales (tens of minutes at 0 V), the relevant mechanism is therefore charge transfer/back-transfer between oxygen vacancy states and neighboring Hf 5*d* orbitals ($Hf^{4+} \leftrightarrow Hf^{3+}$), rather than ongoing injection or long-range transport across the film.

The change in SBH with polarization, $\Delta\varphi_{(B,n)}$ allows accessing the effective screening length via Eq.1. Using $2P_r$=35 $\mu C.cm^{-2}$ and the measured $\Delta\varphi_{(B,n)}$= 0.3 eV, the λ_{eff} is 0.04 Å. The value is similar to the typical effective screening length of 0.07 Å calculated for the Au/PMN-PT interface[17]. The lower value obtained here may be due to the screening contribution of the oxynitride interface layer and to the effectiveness of the charge redistribution at the two TiN/HZLO interfaces due to the density of $V_{\ddot{O}}$[24].

In conclusion, HAXPES was used to probe the link between $V_{\ddot{O}}$ profile and imprint in fully woken-up HZLO capacitors. Imprint values measured within 30 minutes and the low activation energy (∼0.1 eV) indicate a fast electronic mechanism, primarily charge trapping/detrapping at pre-existing oxygen vacancies. The polarization-dependent modulation of the $V_{\ddot{O}}$ depth profile reflects redistribution of electronic charge without physical vacancy motion, stabilizing polarization via internal field modulation. While vacancy drift is absent on this timescale, slower ionic migration may contribute over longer durations, leading to permanent imprint shifts. Very fast injection may occur during the switching pulse (ms range) and likely sets the initial trap occupancy. Future time-resolved photoemission with higher temporal resolution could separate these contributions over timescales from 1 to 10^5 s. The observed polarization-dependent Schottky barrier height supports the imperfect screening model, underscoring the importance of controlling $V_{\ddot{O}}$ density and interface quality for improved reliability.

The Supplemental Material includes a quantitative depth-profile simulation of $V_{\ddot{O}}$ based on Hf^{3+} fractions from the HAXPES data and a description of the method used to determine the Schottky barrier height.

This project has received funding from the European Union's Horizon 2020 research and innovation programme under grant agreement 780302 3εFERRO. The synchrotron radiation experiments were performed with the approval of the Japan Synchrotron Radiation Research Institute (JASRI, proposal no. 2020A4908). We acknowledge access to the Nanofabrication platform at CEA/SPEC. The data that sup-

port the findings of this study are available from the corresponding author upon reasonable request.

[1] T. S. Böscke, J. Müller, D. Bräuhaus, U. Schröder, and U. Böttger, Applied Physics Letters **99**, 102903 (2011).
[2] W. Banerjee, A. Kashir, and S. Kamba, **18**, 2107575 (2022).
[3] H. Mulaosmanovic, E. T. Breyer, S. Dünkel, S. Beyer, T. Mikolajick, and S. Slesazeck, Nanotechnology **32**, 502002 (2021).
[4] E. Covi, H. Mulaosmanovic, B. Max, S. Slesazeck, and T. Mikolajick, Neuromorphic Computing and Engineering **2**, 12002 (2022).
[5] T. Mikolajick, S. Slesazeck, M. H. Park, and U. Schröder, MRS Bulletin **43**, 340 (2018).
[6] R. Alcala, F. Mehmood, P. Vishnumurthy, T. Mittmann, T. Mikolajick, and U. Schröder, 2022 IEEE International Memory Workshop, IMW 2022 - Proceedings , 31 (2022).
[7] S. Lancaster, P. D. Lomenzo, M. Engl, B. Xu, T. Mikolajick, U. Schröder, and S. Slesazeck, Frontiers in Nanotechnology **4**, 939822 (2022).
[8] F. Mehmood, M. Hoffmann, P. D. Lomenzo, C. Richter, M. Materano, T. Mikolajick, and U. Schröder, Advanced Materials Interfaces **6**, 1 (2019).
[9] P. Yuan, G-Q. Mao, Y. Cheng, K-H. Xue, Y. Zheng, Y. Yang, and P. Jiang, Nano Res. **15**, 3667 (2022).
[10] M. Pešić, F. P. G. Fengler, L. Larcher, A. Padovani, T. Schenk, E. D. Grimley, X. Sang, J. M. LeBeau, S. Slesazeck, U. Schröder, and T. Mikolajick, Advanced Functional Materials **26**, 4601 (2016).
[11] A. Jan, T. Rembert, S. Taper, J. Symonowicz, N. Strkalj, T. Moon, Y. S. Lee, H. Bae, H. J. Lee, D. H. Choe, J. Heo, J. MacManus-Driscoll, B. Monserrat, and G. Di Martino, Advanced Functional Materials **33**, 2214970 (2023).
[12] D. R. Islamov, V. A. Gritsenko, T. V. Perevalov, V. A. Pustovarov, O. M. Orlov, A. G. Chernikova, A. M. Markeev, S. Slesazeck, U. Schröder, T. Mikolajick, and G. Y. Krasnikov, Acta Materialia **166**, 47 (2019).
[13] A. Chouprik, D. Negrov, E. Y. Tsymbal, and A. Zenkevich, Nanoscale **13**, 11635 (2021).
[14] C. Zacharaki, P. Tsipas, S. Chaitoglou, L. Bégon-Lours, M. Halter, and A. Dimoulas, Applied Physics Letters **117**, 212905 (2020).
[15] M. Stengel, P. Aguado-Puente, N. Spaldin, and J. Junquera, Physical Review B **83**, 235112 (2011).
[16] A.M. Bratkovsky, and A.P. Levanyuk, arxiv.org/abs/0801.1669 (2008).
[17] E. Kröger, A. Petraru, A. Quer, R. Soni, M. Kalläne, N. a. Pertsev, H. Kohlstedt, and K. Rossnagel, Physical Review B - Condensed Matter and Materials Physics **93**, 235415 (2016).
[18] M. Müller, P. Lömker, P. Rosenberger, M. H. Hamed, D. N. Mueller, R. A. Heinen, T. Szyjka, and L. Baumgarten, Journal of Vacuum Science Technology A **40**, 13215 (2022).
[19] E. A. Kraut, R. W. Grant, J. R. Waldrop, and S. P. Kowalczyk, Physical Review Letters **44**, 1620 (1980).
[20] C. S. Fadley, *Springer Series in Surface Sciences*, Vol. **59** (2016) pp. 1–34.
[21] J. E. Rault, G. Agnus, T. Maroutian, V. Pillard, P. Lecoeur, G. Niu, B. Vilquin, M. G. Silly, A. Bendounan, F. Sirotti, and N. Barrett, Physical Review B - Condensed Matter and Materials Physics **87**, 155146 (2013).
[22] Y. Matveyev, V. Mikheev, D. Negrov, S. Zarubin, A. Kumar, E. D. Grimley, J. M. Lebeau, A. Gloskovskii, E. Y. Tsymbal, and A. Zenkevich, Nanoscale **11**, 19814 (2019).
[23] Z. Liu, K. Toprasertpong, Z. Cai, M. Takenaka, and S. Takagi, Applied Physics Letters **125**, 072904 (2024).
[24] W. Hamouda, C. Lubin, S. Ueda, Y. Yamashita, O. Renault, F. Mehmood, T. Mikolajick, U. Schröder, R. Negrea, and N. Barrett, Applied Physics Letters **116**, 252903 (2020).
[25] P. Buragohain, A. Erickson, P. Kariuki, T. Mittmann, C. Richter, P. D. Lomenzo, H. Lu, T. Schenk, T. Mikolajick, U. Schröder, and A. Gruverman, ACS Applied Materials and Interfaces **11**, 35115 (2019).
[26] S. Vecchi, F. M. Puglisi, P. Appelt, R. Guido, X. Wang, S. Slesazeck, T. Mikolajick, and S. Lancaster, Advanced Electronic Materials **11**, 2400204 (2025).
[27] S. Ueda, Y. Katsuya, M. Tanaka, H. Yoshikawa, Y. Yamashita, S. Ishimaru, Y. Matsushita, and K. Kobayashi, AIP Conference Proceedings **1234**, 403 (2010).
[28] S. Tanuma, C. J. Powell, and D. R. Penn, Surface and Interface Analysis **43**, 689 (2011).
[29] N. Fairley, "http://www.casaxps.com/," (2020).
[30] L. Shvilberg, C. Zhou, M. K. Lenox, B. L. Aronson, S. T. Jaszewski, E. J. Opila, N. K. Lam, C. Zhou, M. K. Lenox, B. L. Aronson, N. K. Lam, S. T. Jaszewski, E. J. Opila, and J. F. Ihlefeld, Applied Physics Letters **124**, 2252905 (2024).
[31] Y. A. Matveyev, A. M. Markeev, Y. Y. Lebedinskii, A. A. Chouprik, K. V. Egorov, W. Drube, and A. V. Zenkevich, Thin Solid Films **563**, 20 (2014).
[32] W. Hamouda, A. Pancotti, C. Lubin, L. Tortech, C. Richter, T. Mikolajick, U. Schröder, and N. Barrett, Journal of Applied Physics **127**, 64105 (2020).
[33] M. Pešić, F. L. G. Fengler, L. Larcher, A. Padovani, T. Schenk, E. D. Grimley, X. Sang, J. M. LeBeau, S. Slesazeck, U. Schröder, and T. Mikolajick, Advanced Functional Materials **26**, 4601 (2016).
[34] U. Schröder, C. Richter, M. H. Park, T. Schenk, M. Pešić, M. Hoffmann, F. P. G. Fengler, D. Pohl, B. Rellinghaus, C. Zhou, C. C. Chung, J. L. Jones, and T. Mikolajick, Inorganic Chemistry **57**, 2752 (2018).
[35] L. Azevedo Antunes, S. Obernberger, P. Schwermer, J. Hintz, R. Ganser, U. Schröder, T. Mikolajick, and A. Kersch, Journal of Applied Physics **137**, 1 (2025).
[36] Y. Mi, G. Geneste, J. Rault, C. Mathieu, A. Pancotti, and N. Barrett, Journal of Physics: Condensed Matter **24**, 275901 (2012).
[37] R. Alcala, M. Materano, P. D. Lomenzo, P. Vishnumurthy, W. Hamouda, C. Dubourdieu, A. Kersch, N. Barrett, T. Mikolajick, and U. Schröder, Advanced functional materials **33**, 2303261 (2023).
[38] M. Engl, W. Hamouda, I. Häusler, S. Lancaster, L. Carpentieri, T. Mikolajick, C. Dubourdieu, and S. Slesazeck, ACS Applied Materials & Interfaces **17**, 51468 (2025).
[39] N. Barrett, W. Hamouda, C. Lubin, J. Laguerre, C. Carabasse, N. Vaxelaire, J. Coignus, S. Martin, and L. Grenouillet, Applied Physics Letters **125**, 43502 (2024).
[40] W. Hamouda, F. Mehmood, T. Mikolajick, U. Schröder, T. O. Mentes, A. Locatelli, and N. Barrett, Applied Physics Letters **120**, 202902 (2022).